ISSN 1027-4510, Journal of Surface Investigation: X-ray, Synchrotron and Neutron Techniques, 2018, Vol. 12, No. 2, pp. 287–296. © Pleiades Publishing, Ltd., 2018.
Original Russian Text © A.N. Khodan, G.P. Kopitsa, Kh.E. Yorov, A.E. Baranchikov, V.K. Ivanov, A. Feoktystov, V. Pipich, 2018, published in Poverkhnost', 2018, No. 4, pp. 00000–00000.

Structural Analysis of Aluminum Oxyhydroxide Aerogel by Small Angle X-Ray Scattering

A. N. Khodan[a, *], G. P. Kopitsa[b, c], Kh. E. Yorov[d], A. E. Baranchikov[e], V. K. Ivanov[e, f], A. Feoktystov[g], and V. Pipich[g]

[a] *Frumkin Institute of Physical Chemistry and Electrochemistry, Russian Academy of Sciences, Moscow, 119071 Russia*
[b] *Konstantinov Petersburg Nuclear Physics Institute, National Research Center "Kurchatov Institute", Gatchina, 188300 Russia*
[c] *Grebenshchikov Institute of Silicate Chemistry, Russian Academy of Sciences, St.-Petersburg, 199034 Russia*
[d] *Moscow State University, Moscow, 119991 Russia*
[e] *Kurnakov Institute of General and Inorganic Chemistry, Russian Academy of Sciences, Moscow, 119071 Russia*
[f] *National Research Tomsk State University, Tomsk, 634050 Russia*
[g] *Jülich Centre for Neutron Science, Forschungszentrum Jülich GmbH, Outstation at MLZ, Garching, Germany*
**e-mail: anatole.khodan@gmail.com*

Received July 22, 2017

Abstract—The work presents studies on the microstructure and mesostructure of nanostructured aluminum oxyhydroxide formed as a high porous monolithic material through the surface oxidation of aluminum liquid-metal solution in mercury in a temperature- and humidity-controlled air atmosphere. The methods of X-ray diffraction analysis, thermal analysis, the low temperature adsorption of nitrogen vapors, transmission electron microscopy, small-angle and very small-angle neutron scattering, and small-angle X-ray scattering are used for comprehensive investigation of the samples synthesized at 25°C as well as that annealed at temperatures up to 1150°C. It is found that the structure of the monolithic samples can be described within the framework of a three-level model involving primary heterogeneities (typical length scale of $r_c \approx 9–19$ Å), forming fibrils (cross-sectional radius $R \approx 36–43$ Å and length $L \approx 3200–3300$ Å) or lamellae (thickness $T \approx 110$ Å and width $W \approx 3050$ Å) which, in turn, are integrated into large-scale aggregates (typical size $R_c \approx 1.25–1.4$ μm) with an insignificant surface roughness. It is shown that a high specific surface (~200 m^2/g) typical for the initial sample is maintained upon its thermal annealing up to 900°C, and it decreases to 100 m^2/g after heat treatment at 1150°C due to fibrillary agglomeration.

Keywords: nanostructured aluminum oxyhydroxide, aerogels, small-angle neutron scattering, small-angle X-ray scattering

DOI: 10.1134/S102745101802026X

INTRODUCTION

It has been long known that the air oxidation of metal aluminum in the presence of mercury leads to the formation of loose oxides and the fast fracture of aluminum products [1]. The result of oxidation is a nanostructured aluminum oxyhydroxide (NAO) characterized by a fibrillary structure and extremely low density (~0.013 g/cm^3), which makes it possible to consider it as a one-dimensional (1D) aerogel. The preparation of 1D aerogels is a an area of research currently under development; in particular, materials based on tungsten oxide [2], titanates and manganites of alkali metals [3], metallic copper [4], and carbon nanotubes [5] are described in publications.

The main problem in producing NAO-based monolithic materials lies in achieving permanent rates of aluminum oxidation and the growth of fibrils which is primarily determined by the aluminum content in a liquid-metal phase as well as ambient temperature and humidity. Recent systematic research [6–9] revealed the optimal conditions of the reproducible preparation of NAO aerogel monolithic samples of a preset arbitrary cross-sectional shape containing holes with a specified diameter. Vignes et al. analyzed in detail the formation mechanism of these materials as well as the key regularities of changes in some of their physicochemical characteristics (specific surface, chemical and phase compositions, geometric density) upon heat treatment within a wide range of temperatures (up to 1650°C) [8].

Despite the applicability of NAO materials (chemical inertness, extremely low density, high specific surface area and high mechanical strength of monolithic samples with a porosity of 98%), the number of publications related to the synthesis and analysis of the physicochemical characteristics of these materials is

insignificant. Notably, the formation mechanism of NAO fibrils upon the selective oxidation of aluminum on an amalgam surface is, as yet, an unexplored area. The correct description as well as identification of the features of structural transformations occurring during the heat treatment of NAO requires detailed information on the structure of these materials in a wide range of scales.

The objective of the work is comprehensive analysis of the peculiarities of the microstructure and mesostructure of NAO, as well as its evolution upon heat treatment. For our investigations we apply three scattering techniques: small-angle neutron scattering (SANS), very small-angle neutron scattering (VSANS), and small-angle X-ray scattering (SAXS), which provide most of the structural data.

EXPERIMENTAL

The NAO monolithic samples were synthesized in accordance with a procedure described in detail previously [8]. The obtained aerogels were subjected to thermal annealing at 450, 900 and 1150°C in air in a muffle furnace (heating rate was 10 grad/min, isothermal time was 1 h). Before all measurements the samples were ground in an agate mortar.

X-ray diffraction analysis of the samples was carried out using a Bruker D8 Advance (CuK_α-radiation) diffractometer within the 2θ range from 5° to 80° with a step width of 0.02°. The X-ray patterns were decoded using the ICDD PDF2 database. Analysis of the samples by transmission electron microscopy (TEM) was carried out using a Leo 912 AB Omega microscope operating at an accelerating voltage of 100 kV.

The specific surface and pore size distribution were determined using the low temperature adsorption of nitrogen using a QuantaChrome Nova 4200B analyzer. The samples were degassed at 120°C in vacuum for 16 h. On the basis of the data obtained, the specific surface area S_{BET} was determined using the Brunauer-Emmett-Teller (BET) method over seven points. The pore size distribution was calculated from the isotherms of nitrogen desorption using the Barrett–Joyner–Halenda (BJH) model.

Thermal analysis of the samples was carried out by the application of an SDT Q-600 analyzer (TA Instruments) at temperatures up to 1300°C at a heating rate of 10 grad/min in air flow (250 mL/min). The mass of the samples was ~60 mg.

The SANS and VSANS measurements were carried out on KWS-2 and KWS-3 instruments (an FRM-II reactor in Garching, Germany), correspondingly. The KWS-2 instrument is a classic small-angle diffractometer operating in near point geometry. The measurements were carried out at a neutron wavelength of $\lambda = 5.2$ Å with $\Delta\lambda/\lambda = 0.1$. Using three sample–to-detector distances (2, 8 and 20 m), the neutron scattering intensity in the momentum transfer q range between 3×10^{-3} and 0.43 Å^{-1} was measured. Scattered neutrons were detected using a two-dimensional position-sensitive detector with a ^{6}Li glass scintillator (128 × 128 cells with a spatial resolution of 5 × 5 mm).

The KWS-3 instrument is a small-angle diffractometer operating with a focusing toroidal mirror that allows the attainment of a high resolution by transmitted momenta q up to 1×10^{-4} Å^{-1} [10, 11]. The measurements were carried out at a neutron wavelength of $\lambda = 12.8$ Å ($\Delta\lambda/\lambda = 0.2$). Two sample-to-detector distances (1 and 10 m) were used allowing measurements to be carried out within a range of q between 4×10^{-4} and 1.4×10^{-2} Å^{-1}. Scattered neutrons were detected using a two-dimensional position-sensitive detector with a ^{6}Li glass scintillator (diameter of the active zone was 8.7 cm; spatial resolution was 0.36 × 0.39 mm).

The powders under study were placed between two quartz-glass plates. The initial spectra for each q range were corrected using a standard procedure [12] for scattering from the carcass of the instrument and quartz glasses as well as for the background. The obtained two-dimensional isotropic spectra were azimuthally averaged and calibrated in absolute units through normalization to an incoherent scattering cross section of a Plexiglas standard sample with account taken of the detector efficiency [12] and the length L for each sample. All measurements were performed at room temperature. The QtiKWS software was used for preliminary data processing [13].

The SANS and VSANS intensity $I_s(q)$ analyzed in the work was determined as

$$I_s(q) = I(q) - TI_0(q), \quad (1)$$

where $I(q)$ and $I_0(q)$ is the q distribution of scattered neutrons after a sample and a neutron beam without a sample, correspondingly; T is the transmission coefficient of neutrons passed through a sample:

$$T = \frac{I(0)}{I_0(0)} = \exp(-\Sigma_{tot} L), \quad (2)$$

where $\Sigma = \sigma_s + \sigma_a$ is the integral section including nuclear scattering σ_s and absorption σ_a; L is the thickness of the sample.

The measured values of the SANS and USANS intensity are related to the scattering law $S(q)$ through the following equation:

$$I_s(q) = I_0 L \int F(q - q_1) S(q) dq_1, \quad (3)$$

where $F(q)$ is the function of the instrumental resolution which was approximated by a Gaussian function [14].

Therefore, the use of a combination of VSANS and SANS techniques enabled us to make an analysis in the momentum-transfer range of $2 \times 10^{-4} < q < 0.43$ Å^{-1}, which corresponded to a range of characteristic dimensions from 10 Å to several microns.

The SAXS measurements were carried out at the experimental station DIXI situated on the 1.3.a. line of the KCSR-Kurchatov synchrotron (Scientific Research Center "Kurchatov Institute", Moscow) operating in the axial geometry and equipped with a MarCCD 165 (Rayonix) gas-filled detector with a diameter of the active zone of 190 mm and resolution of 80 μm. Use of the photon wavelength $\lambda = 1.62$ Å and two sample-detector distances (600 and 2430 mm) enabled us to measure the scattering intensity covering the momentum-transfer range of $4 \times 10^{-3} \le q \le 4 \times 10^{-1}$ Å^{-1}. Before the measurements, the powders were poured onto adhesive tape. The initial spectra were corrected for scattering from the carcass and the tape as well as for the background. The obtained two-dimensional isotropic spectra were azimuthally averaged taking into account the detector efficiency. All the measurements were carried out at room temperature. The fit2D (ESRF) software package was used for preliminary data processing [15].

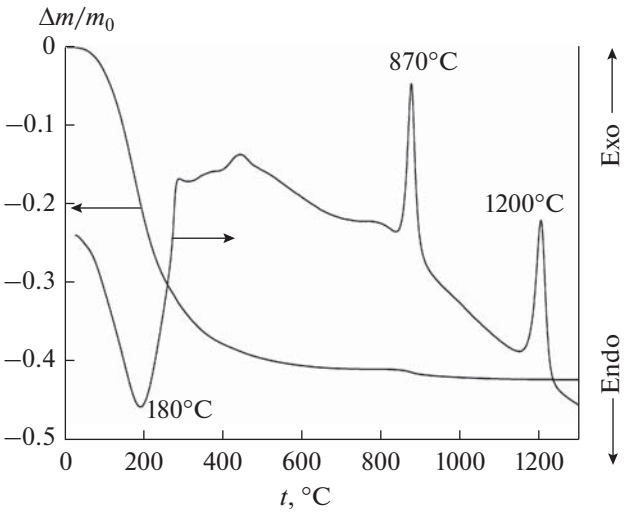

Fig. 1. Results of thermogravimetric and differential thermal analysis of the initial NAO sample.

RESULTS AND DISCUSSION

The initial NAO sample is a highly fragile material, and heat treatment of the NAO monolithic material leads to its shrinkage, and the geometric sizes of the sample decreased approximately twice upon annealing at 1150°C; although the integrity of the samples remained unchanged.

The thermal analysis of NAO (Fig. 1) revealed a two-stage process of its thermal destruction. The first stage of thermolysis (maximum rate of mass loss at 180°C) is responsible for the removal of weakly bound water; the corresponding mass loss accounted for ~40.8%. The second stage of mass loss (maximum rate at 870°C, $\Delta m/m_0 = 1.3\%$) is accompanied by an exothermal effect related to the crystallization of aluminum oxide. Further heating of the sample up to 1300°C proceeded without any mass loss; however, at 1200°C the exothermal effect likely associated with the crystallization of corundum was observed [8]. The chemical composition of the initial NAO sample derived from the data of thermal analysis corresponds to the gross formula of $Al_2O_3 \cdot 4.12H_2O$.

The XRD data of the initial NAO sample as well as the samples subjected to treatment at 450, 900 and 1150°C are given in Fig. 2. As follows from Fig. 2, the phase composition of the initial aerogel is identical to that of the sample produced through treatment at 450°C and corresponds to the X-ray amorphous phase. When the annealing temperature increased to 900 and 1150°C, a cubic modification of aluminum oxide γ-Al_2O_3 was formed (PDF2 77-396, space group $Fd\bar{3}m$). Estimation of the areas of coherent scattering for the obtained samples of γ-Al_2O_3 in accordance with the Scherrer formula (for the reflection 400) gave a value of about 4 nm. It should be noted that nanocrystalline γ-Al_2O_3 is generally regarded as one of the

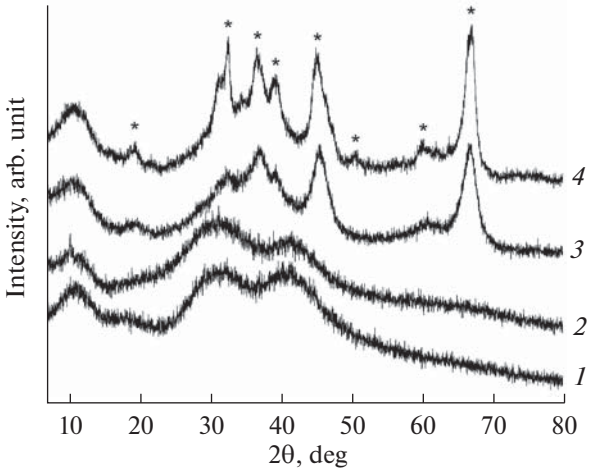

Fig. 2. XRD patterns of the NAO samples: initial sample (*1*) and the products of its annealing at 450 (*2*), 900 (*3*) and 1150°C (*4*). The reflections attributed to the γ-Al_2O_3 phase are denoted by an asterisk.

best catalysts for hydrogen conversion [16]. The obtained data are in agreement with the results of analysis of the phase transformations of NAO at high temperatures [8].

Based on data available from thermal analysis (Fig. 1) and XRD experiments (Fig. 2), the scheme of thermal transformations of NAO (up to 1300°C) can be described as follows:

$$Al_2O_3 \cdot 4.12H_2O \text{ (amorph.)}$$
$$\xrightarrow{800^\circ C} Al_2O_3 \cdot 0.22H_2O \text{ (amorph.)}$$
$$\xrightarrow{870^\circ C} \gamma\text{-}Al_2O_3 \xrightarrow{1200^\circ C} \alpha\text{-}Al_2O_3.$$

Figure 3 shows the TEM images of the initial NAO sample as well as the products of its heat treatment. It can be seen that the initial NAO sample consists of

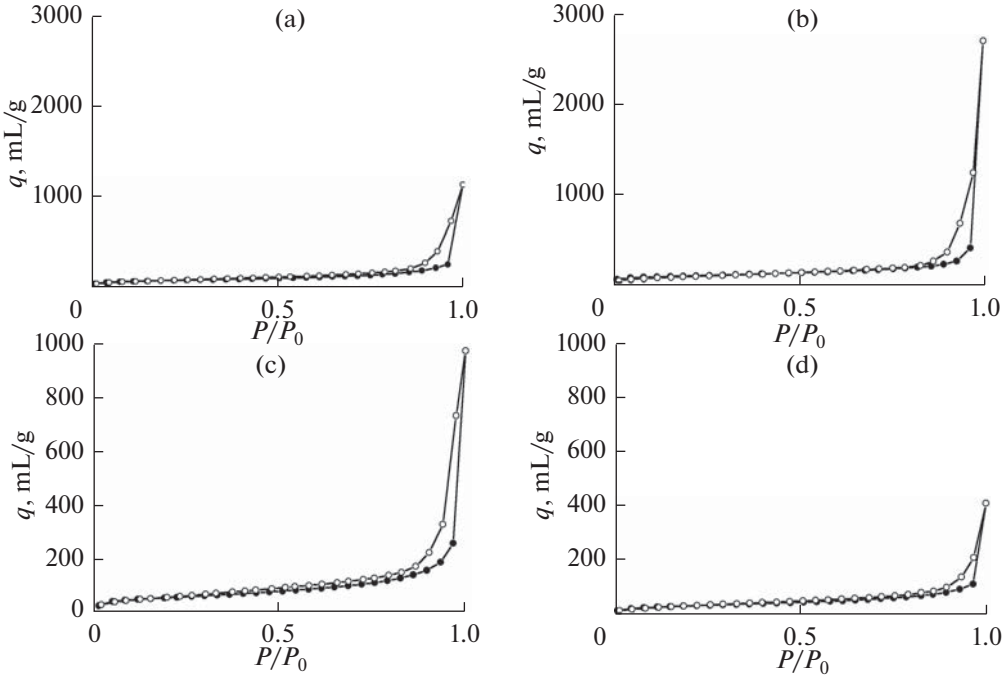

Fig. 3. TEM data and electron diffraction pattern for the samples of the initial NAO (a) and the products of its annealing at 450 (b), 900 (c), and 1150°C (d).

intertangled fibrils with a diameter of ~10 nm. High temperature annealing does not lead to any significant changes in the structure, but treatment at 1150°C results in the enlargement of particles up to ~20 nm. The electron diffraction pattern observed for the samples annealed at 900 and 1150°C is typical for crystalline substances and entirely consistent with the XRD data.

Figure 4 shows the isotherms of nitrogen adsorption and desorption for all the samples under study. The isotherms are similar in appearance to that of the second type according to the classification originally proposed by Brunauer, Deming, Deming and Teller [17], which corresponds to nonporous and macroporous adsorbents. At the same time, the presence of a hysteresis loop is indicative of the fourth type which characterizes mesoporous adsorbents. According to the De-Boer classification [18], the shape of the hysteresis loop in all cases corresponds to the *C* type which is associated with wedge-shaped pores with open ends. The hysteresis loops started closing at the relative pressures $P/P_0 > 0.3$, which is indicative of an insignificant quantity of micropores in the samples. Table 1 and Figure 5 demonstrate the results of analyzing the obtained isotherms with the use of the BET and BJH models.

As follows from Table 1, the initial NAO sample possesses a high specific surface (S_{BET} = 220 m^2/g). Annealing at 450°C leads to a significant increase in S_{BET} (of ~20%) and a twofold increase in the specific pore volume which is obviously connected with the topochemical removal of chemically bound water. A further increase in the annealing temperature reduces S_{BET} to 190 (900°C) and 100 m^2/g (1150°C), apparently due to alumina particle sintering and changes in the shape of fibrils.

The data available within the BJH model indicate the bimodal pore size distribution in all the samples under study (Fig. 5); the maximal specific pore volumes correspond to pore diameters of ~24 and ~2 nm. It should be noted that the increase in the annealing temperature has virtually no effect on the positions of peaks, nor the pore size distributions. Moreover, the relative contents of large and small mesopores remain relatively constant up to 900°C which is indicative of the high stability of the NAO mesostructure in this temperature range. The fraction of large mesopores decreases significantly at higher temperatures (1150°C), although mesopores with a small diameter persist providing a relatively high specific surface of the material (~100 m^2/g).

Let us consider the results of SAXS and SANS analysis of the initial NAO sample and the products of NAO heat treatment in more detail. Figure 6 shows the experimental log-log plot of neutron scattering cross sections $d\Sigma(q)/d\Omega$ versus the momentum transfer q for all samples under study. It can be seen that when the momentum transfer is large ($q > 0.2$ Å^{-1}), the maximum intensity of neutron scattering is observed for the initial (unannealed) NAO sample, which is apparently due to incoherent scattering from hydrogen

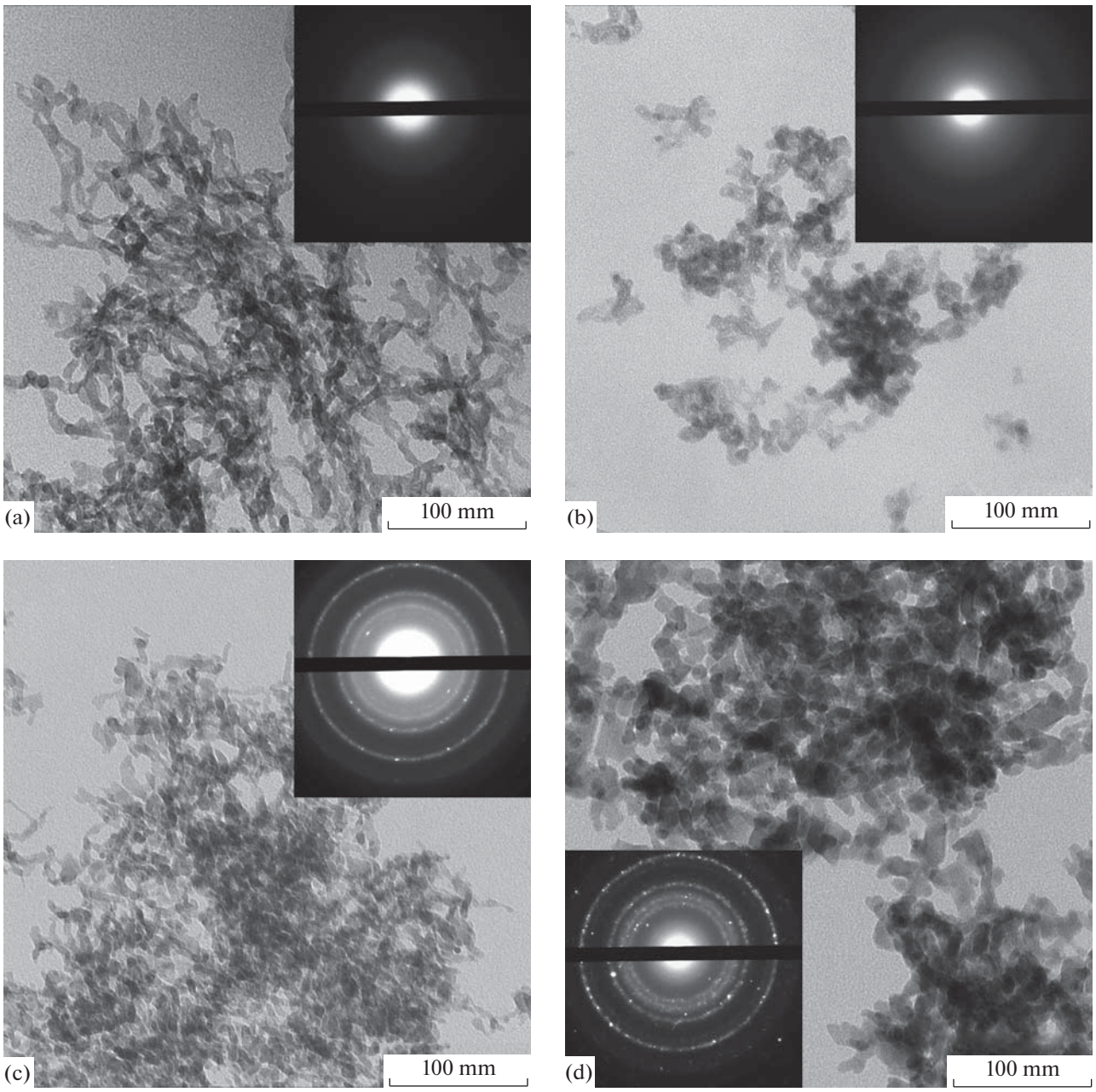

Fig. 4. Isotherms of nitrogen adsorption and desorption on the initial NAO (a) and the products of its heat treatment at 450 (b), 900 (c) and 1150°C (d).

atoms contained in NAO in the form of chemically bound or adsorbed water. However, a direct correlation between the annealing temperature and the intensity of neutron scattering is observed for the other momentum transfers. The large intensity of neutron scattering in the sample produced through annealing at 450°C is due to the high value of its specific surface (Table 1). The value of S_{sp} is included in the expression for the neutron-scattering cross section $d\Sigma(q)/d\Omega$ as a linear term [19]. The higher intensity of scattering in the samples produced through annealing at 900 and

Table 1. Specific surface (S_{BET}) and specific pore volume (V_{BJH}) determined by the method of the adsorption/desorption of nitrogen on NAO and the products of NAO annealing

t, °C	S_{BET}, m^2/g	V_{BJH}, cm^3/g
–	220 ± 10	1.75
450	265 ± 15	3.31
900	190 ± 10	1.51
1150	100 ± 10	0.63

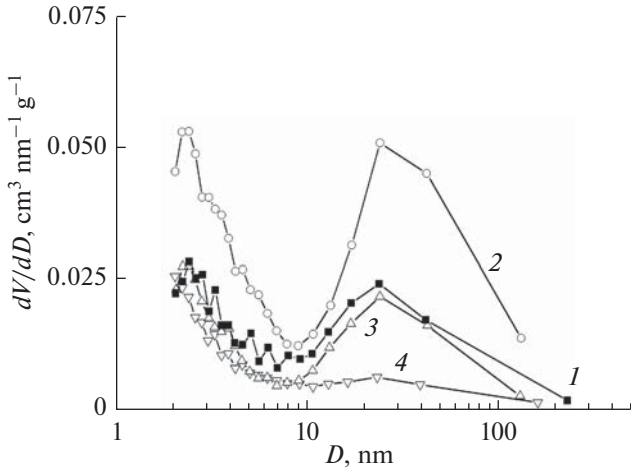

Fig. 5. Pore size distribution calculated with the use of the BJH model for the initial NAO sample (*1*) and the products of its annealing at 450 (*2*), 900 (*3*), and 1150°C (*4*).

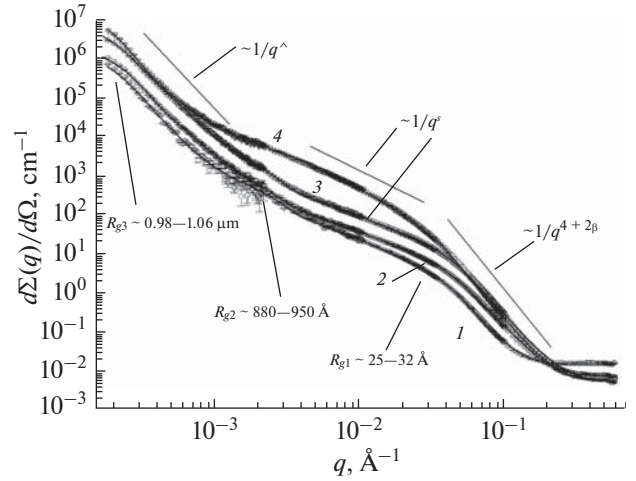

Fig. 6. Dependence of the differential SANS and VSANS cross sections $d\Sigma(q)/d\Omega$ on the momentum transfer q for the initial NAO sample (*1*) and the products of its annealing at 450 (*2*), 900 (*3*), and 1150°C (*4*). Solid lines are the data fitting in accordance with Eqs. (6) and (7).

1150°C is apparently caused by the presence of a crystalline phase.

Common to all the scattering curves shown in Fig. 6 is the presence of two ranges within which the scattering cross sections $d\Sigma(q)/d\Omega$ follow the power laws $q^{-\Delta}$ with various power exponents Δ. The first of these ($\Delta = n_1$) is found within the range of relatively large momentum transfers ($4.5 \times 10^{-2} < q < 2 \times 10^{-1}$ Å^{-1}), the second one ($\Delta = n_2$) is within the range of $2.5 \times 10^{-4} < q < 1 \times 10^{-3}$ Å^{-1}. In the intermediate region of $1 \times 10^{-3} < q < 4.5 \times 10^{-2}$ Å^{-1} as well as for $q < 2.5 \times 10^{-4}$ Å^{-1}, the dependence of the scattering cross section $d\Sigma(q)/d\Omega$ is satisfactorily described within the framework of the generalized Guinier approximation [20–23].

Thus, the SANS pattern observed for all samples is typical for all systems with disordered or, as in this case, porous (solid phase-pore) structure, and is indicative of two types of scattering heterogeneities which differ drastically in characteristic scale, i.e., the samples possess a two-level hierarchical structure [24–27]. These materials most probably involve the large-scale heterogeneities composed of primary heterogeneities having an aspherical shape.

The SANS pattern at a smaller structural scale corresponding to the range of $q > 1 \times 10^{-3}$ Å^{-1} (Fig. 6) is typical for randomly oriented aspherical (anisodiametric) objects, for example, for extremely stretched (fibrils) or flattened (lamella) particles. To describe scattering in the Guinier region in which it is determined by the characteristic size R_c and shape of independent scattering heterogeneities and not their local structure, it is necessary to use the generalized expression [28]:

$$\frac{d\Sigma(q)}{d\Omega} = \frac{G}{q^s}\exp\left(-\frac{q^2R_g^2}{3-s}\right), \quad (4)$$

where amplitude G is proportional to the production of a number of heterogeneities in a scattering volume and the average density ρ of the neutron scattering amplitude [20–23], and parameter s is determined by the shape of scattering heterogeneities. For spherical objects: $s = 0$; for one-dimensional particles (fibrils): $s = 1$; for two-dimensional heterogeneities (lamellae): $s = 2$. The values of parameter s can be not only an integer, but fractional as well, for example, if the scattering heterogeneities have the shape of a rotational ellipsoid or the system includes heterogeneities in any one of a number of shapes.

Since aspherical objects are determined by not only one characteristic size but two sizes (radius R_c and length L in the case of fibrils) or three sizes (thickness T, width W and length L for lamella), the corresponding Guinier region can contain two or three ranges of momentum transfer q, which is entirely in line with the observed experimental data (Fig. 6). For all the powders under study, three regions can be distinguished on the dependences of the scattering cross sections at $q > 1 \times 10^{-3}$ Å^{-1}: the region related to the Porod regime, where scattering is determined by the local structure of scattering heterogeneities and described by the power dependence q^{-n_1}; and two regions corresponding to the Guinier regime, where scattering is determined by the characteristic sizes of aspherical scattering heterogeneities.

The values of the power exponent n_1 determined from the slope of the linear parts of the experimental dependences $d\Sigma(q)/d\Omega$ are within the range from 4.21 to 4.69. The indicated values are typical for porous systems with a diffuse interface, $n = 4 + 2\beta > 4$, where

$0 \le \beta \le 1$ is the parameter which determines the law of variations in the nuclear density ρ in the surface layer of scattering heterogeneities [29]. On the assumption that these heterogeneities possess a smooth surface, the nuclear density ρ would depend only on the distance x from a point on the surface. Therefore, the nuclear density $\rho(x)$ can be expressed as follows:

$$\begin{cases} \rho(x) = 0, & x < 0 \\ \rho(x) = \rho_0 (x/\alpha)^{\beta}, & 0 \le x \le \alpha, \\ \rho(x) = \rho_0, & x \le \alpha \end{cases} \quad (5)$$

where α is the thickness of the diffusion layer where the nuclear density ρ increases from 0 to ρ_0. This model can be used for the further analysis of neutron scattering in the range of $q > 1 \times 10^{-3}$ Å^{-1} [29].

For $q > 2 \times 10^{-1}$ Å^{-1}, the scattering cross section $d\Sigma(q)/d\Omega$ ceases to depend on q and likely corresponds to incoherent scattering from hydrogen atoms making it impossible to examine the scattering process in this region. In this regard, additional examination by means of SAXS was carried out; the SAXS data will be discussed below.

In general, the analysis of scattering at the first structural level (in the range of $q > 1 \times 10^{-3}$ Å^{-1}), which is characterized by the smallest characteristic size, relies on the generalized empirical Guinier-Porod model [28]:

$$\frac{d\Sigma(q)}{d\Omega} = G_2 \exp\left(-\frac{q^2 R_{g2}^2}{3}\right) \text{ at } q < q_2,$$

$$\frac{d\Sigma(q)}{d\Omega} = \frac{G_1}{q^{s_1}} \exp\left(-\frac{q^2 R_{g1}^2}{3 - s_1}\right) \text{ at } q_2 < q < q_1, \quad (6)$$

$$\frac{d\Sigma(q)}{d\Omega} = \frac{B_1}{q^{n_1}} + I_{\text{inc}} \text{ at } q > q_1.$$

Here, $(3 - s_1)$ is the dimensional factor; R_{g1} and R_{g2} are the characteristic sizes of aspherical scattering heterogeneities ($R_{g1} < R_{g2}$) (for fibrils with the radius R and length L: $R_{g2} = (L^2/12 + R^2/2)^{1/2}$, $R_{g1} = R/2^{1/2}$; for lamella with the thickness T and width W: $R_{g2} = (W^2/12 + T^2/12)^{1/2}$, $R_{g1} = T/12^{1/2}$); G_2 and G_1 are the Guinier coefficients [20–23]; B_1 is a coefficient determined by the local structure of scattering heterogeneities [30]; and I_{inc} is a constant determined by incoherent scattering from hydrogen atoms.

The analysis of scattering at the second structural level with higher sizes observed in the range of small momentum transfer ($2.5 \times 10^{-4} < q < 1 \times 10^{-3}$ Å^{-1}) is based on the power function q^{-n_2}. The values of the power exponent n_2 determined from the slope of the linear parts of the experimental curves $d\Sigma(q)/d\Omega$ varied within the range from 3.85 to 3.92. These values indicate that in this region of q the scattering law is close to the Porod law ($n = 4$) [31, 32] which corresponds to heterogeneities with a practically smooth surface. An insignificant deviation of the power exponent n_2 from four can be associated either with the presence of scattering at rough heterogeneities with a characteristic size exceeding the wavelength of neutrons used in our experiments (λ = 12.8 Å) [33] or the polydispersity of scattering heterogeneities [34].

Deviation of the experimental dependence of the scattering cross section $d\Sigma(q)/d\Omega$ from the power law q^{-n_2} is observed for all samples when the momentum transfers are small ($q < 2.5 \times 10^{-4}$ Å^{-1}) and is caused by the onset of the Guinier regime where scattering is determined by the characteristic size R_{c3} of independently scattering large-scale heterogeneities. In the case of spherical particles, the relationship $R_c = \sqrt{5/3} R_g$ holds true [35].

Thus, to describe the experimental data in the range of $q > 1 \times 10^{-3}$ Å^{-1}, a unified exponential-power expression was used [36]:

$$\frac{d\Sigma(q)}{d\Omega} = G_3 \exp\left(-\frac{q^2 R_{g3}^2}{3}\right) + \frac{B_2}{\hat{q}^{n_2}}, \quad (7)$$

where $\hat{q} = q/[\text{erf}(qR_g/6^{1/2})]^3$ is the momentum transfer q normalized to the error function erf(x). This procedure allows us to describe correctly the behaviors of the scattering cross section $d\Sigma(q)/d\Omega$ within the intermediate range between $qR_c < 1$ (the Guinier approximation) and $qR_c \gg 1$ (the q^{-n} scattering power law).

To obtain the final results, Eqs. (6) and (7) were convoluted with the instrumental resolution function. The experimental dependences of the differential scattering cross section $d\Sigma(q)/d\Omega$ were processed using the least squares method throughout the entire range under study. The results of analysis are shown in Fig. 6 and Table 2.

As follows from Table 2, all the samples under study constitute a porous system with two-level hierarchical structure. The primary structural level consists of anisodiametric heterogeneities with s characteristic size of $R_{g1} \approx 25$–32 Å possessing a diffuse surface [29]. In the case of the initial NAO and the products of its heat treatment at 450 and 900°C, the value of parameter s is on the order of unity ($s = 1.35$–1.42), which is indicative of the similarity of their shape to fibrils. The radius of the cross section of these fibrils amounts to $R_1 = 2^{1/2} R_{g1} \approx 36$–$43$ Å, and the length $L \approx 3200$–3300 Å, this being consistent with both the TEM results (Fig. 3) and data from publications [8]. The situation is somewhat different in the sample produced by annealing at 1150°C, the corresponding value of parameter s amounts to 1.80, which is more consistent with a lamellar structure (geometric parameters of the lamellae are $T = 12^{1/2} R_{g1} \approx 110$ Å and $W \approx 3050$ Å) but not to a fibrillary structure. The changes in the shape of the scattering heterogeneities of the primary struc-

Table 2. Parameters of the microstructure and mesostructure of the initial NAO and the products of NAO annealing derived from the analysis of VSANS and SANS data

t, °C	–	450	900	1150
Primary structural level (SANS)				
G_2, 10^4 cm^{-1}	0.09 ± 0.01	0.11 ± 0.01	0.38 ± 0.04	1.2 ± 0.06
R_{g2}, Å	952 ± 37	927 ± 42	953 ± 31	880 ± 40
G_1, cm^{-1} Å$^{-s_1}$	0.11 ± 0.01	0.27 ± 0.01	0.34 ± 0.01	0.18 ± 0.01
s_1	1.42 ± 0.01	1.36 ± 0.01	1.35 ± 0.01	1.80 ± 0.01
R_{g1}, Å	30.3 ± 0.5	25.4 ± 0.5	26.2 ± 0.4	32.0 ± 0.6
B_1, 10^{-6} cm^{-1} Å$^{-n_1}$	1.5 ± 0.1	30.0 ± 0.9	8.7 ± 0.4	6.0 ± 0.3
$n_1 = 4 + 2\beta$	4.67 ± 0.03	4.34 ± 0.03	4.69 ± 0.03	4.21 ± 0.03
I_{inc}, 10^{-2} cm^{-1}	1.3 ± 0.1	0.7 ± 0.02	0.7 ± 0.02	0.75 ± 0.02
Secondary structural level (VSANS)				
G_3, 10^7 cm^{-1}	0.21 ± 0.02	0.27 ± 0.01	0.75 ± 0.03	1.64 ± 0.04
R_{g3}, Å	10640 ± 290	9985 ± 120	9770 ± 160	10870 ± 130
B_2, 10^{-9} cm^{-1} Å$^{-n_2}$	2.0 ± 0.5	22.1 ± 0.9	6.6 ± 0.5	10.2 ± 0.4
n_2	3.87 ± 0.09	3.92 ± 0.05	3.85 ± 0.05	3.88 ± 0.05

tural level are probably caused by an increase in the length/diameter ratio for alumina particles due to their sintering.

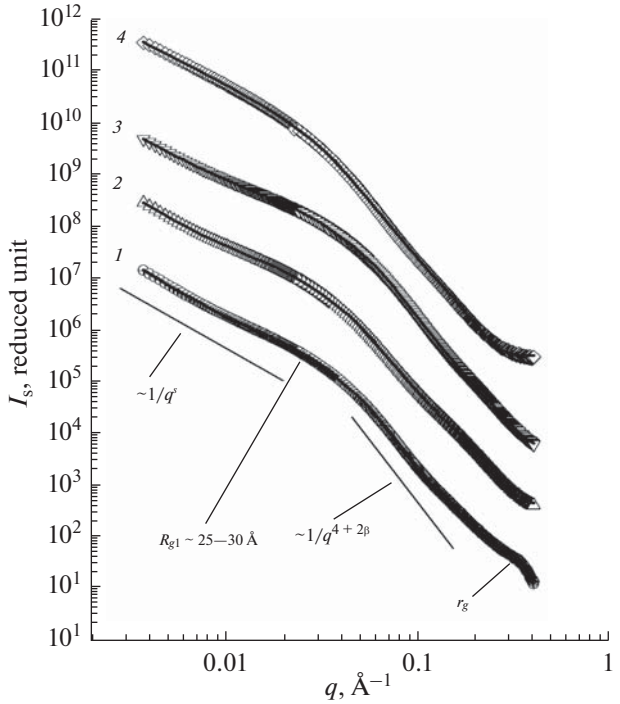

Fig. 7. SAXS data for the initial NAO sample (*1*) and the products of its annealing at 450 (*2*), 900 (*3*), and 1150°C (*4*). Solid lines are the data fitting in accordance with Eq. (8). For illustrative purpose, the values of $I_s(q)$ of the scattering curves *2*, *3*, and *4* were multiplied by 10, 100 and 10000, correspondingly.

Aggregates of scattering heterogeneities constitute the secondary structural level: large scale globules ($R_c = (5/3)^{1/2}$, $R_{g3} \approx 1.25$–1.4 μm) which possess a surface with only minor roughness. As follows from the data from Table 2, the characteristic size (R_c) of large-scale globules slightly depends on the conditions of NAO heat treatment and, in all cases, it is about 1 μm. As the annealing temperature increases to 900°C, a gradual reduction (of ~8%) in R_c is observed, but a further increase in the annealing temperatures to 1150°C leads to the growth of R_c. These processes are apparently related to rearrangement of the NAO mesostructure during its heat treatment, dehydration, crystallization, and growth of the particles.

As mentioned above, it was impossible to examine the neutron scattering cross section in the range of $q > 2 \times 10^{-1}$ Å^{-1} due to a high background produced by incoherent scattering from protium. In this regard, the samples were examined by means of SAXS. Figure 7 shows the obtained data as a log-log plot.

As follows from the obtained data, the shape of the SAXS dependences $I_s(q)$ for all the samples coincides in essence with that of SANS in the range of $q < 2 \times 10^{-1}$ Å^{-1}. This could suggest that X-ray scattering is also determined by the presence of randomly oriented anisodiametric objects (fibrils or lamellae). Figure 7 also indicates a shoulder in the scattering curves in the range of large momentum transfer $q > 2 \times 10^{-1}$ Å^{-1}, which corresponds to the onset of the Guinier regime. In this range, scattering is determined by the characteristic size r_{c0} of independent scattering primary heterogeneities of the basic structural level. It should be noted that with an increase in the annealing tempera-

Table 3. Parameters of the microstruture and mesostructure of the initial NAO and the products of NAO annealing derived from the analysis of SAXS data

t, °C	–	450	900	1150
Primary structural level				
s_1	1.49 ± 0.01	1.43 ± 0.01	1.38 ± 0.01	1.86 ± 0.01
R_{g1}, Å	24.9 ± 0.6	29.4 ± 0.4	25.8 ± 0.4	29.5 ± 0.6
$n_1 = 4 + 2\beta$	4.47 ± 0.04	4.09 ± 0.03	4.36 ± 0.03	4.31 ± 0.03
Basic structural level				
r_g, Å	7.1 ± 0.2	10.8 ± 0.5	11.2 ± 0.4	14.3 ± 0.5

ture the position of this shoulder is regularly shifting towards lower q reflecting an increase in the characteristic size r_{c0}. Thus, the NAO mesostructure, as a whole, is described in terms of the three-level model (basic, primary and secondary structural levels).

In this regard, to examine the SAXS data in the entire range of q, the generalized empirical Guinier-Porod model [28] was used:

$$\frac{d\Sigma(q)}{d\Omega} = \frac{G_1}{q^{s_1}}\exp\left(-\frac{q^2R_{g1}^2}{3-s_1}\right) \text{ at } q < q_1, \quad (8.1)$$

$$\frac{d\Sigma(q)}{d\Omega} = \frac{B_1}{q^{n_1}} + G_0\exp\left(-\frac{q^2r_{g0}^2}{3}\right) \text{ at } q > q_1. \quad (8.2)$$

The experimental dependences of the intensities $I_s(q)$ were processed using the least squares method throughout the entire range of interest. Figure 7 and Table 3 represent the results of the analysis of the SAXS data.

In general, the parameters of the primary structural level derived from the SAXS data are in satisfactory agreement with the SANS results. This applies to the values of parameter s characterizing the shape of scattering heterogeneities, power exponent n_1 characterizing the properties of their surface and parameter R_{g1} which is associated with their characteristic sizes. Some differences in the parameters of the primary structural level determined independently by means of SANS and SAXS are probably due to the contrast of X-ray and neutron scattering from porous objects. Similar observations have been reported recently when analyzing the mesostructure of hydrated zirconium dioxide [37].

According to the SAXS data, the characteristic size r_c of primary heterogeneities increases regularly with growth in the NAO annealing temperature and amounts to 9.2 ± 0.3 Å for the initial NAO material, 13.9 ± 0.7, 14.5 ± 0.6 and 18.5 ± 0.7 Å for the products of its treatment at temperatures of 450, 900 and 1150°C, correspondingly.

CONCLUSIONS

A comprehensive investigation of the microstructure and mesostructure of nanostructured aluminum oxyhydroxide produced through the surface oxidation of an aluminum liquid-metal solution in mercury upon exposure to air as well as the products of its annealing at 450, 900 and 1150°C were carried out for the first time with the use of neutron and X-ray scattering in the momentum transfer range of $2 \times 10^{-4} < q < 0.43$ Å^{-1}. It was found that the structure of the samples under study could be described in terms of a three-level model including primary heterogeneities (characteristic size $r_c \approx 9$–19 Å) forming fibrils (radius of cross section $R \approx 36$–43 Å and length $L \approx 3200$–3300 Å) or lamellae (thickness $T \approx 110$ Å and width $W \approx 3050$ Å) with a diffuse surface, which, in turn, are combined into large-scale aggregates (characteristic size $R_c \approx 1.25$–1.4 μm) with a minor roughness. It was revealed that the NAO fibrillary structure was retained after annealing at temperatures no less than 900°C and violated after heat treatment at 1150°C with a considerable reduction in the specific mesopore volume.

ACKNOWLEDGMENTS

The work was supported by the Russian Foundation for Basic Research, project no. 17-53-150007 NTsNI_a). Investigations were carried out using equipment of the Centers of Collective Use of Physical Methods of the Research of Substances and Materials of the Institute of General and Inorganic Chemistry, Russian Academy of Science.

REFERENCES

1. H. Wislicenus, Z. Chem. Ind. Kolloide **2**, 11 (1908).
2. W. Cheng, F. Rechberger, and M. Niederberger, Nanoscale **8**, 14074 (2016).
3. S. M. Jung, H. Y. Jung, W. Fang, et al., Nano Lett. **14**, 1810 (2014).
4. Y. Tang, S. Gong, Y. Chen, et al., ACS Nano **8**, 5707 (2014).
5. Z. Lin, Z. Zeng, X. Gui, et al., Adv. Energy Mater. **6**, 1600554 (2016).

6. J.-L. Vignes, L. Mazerolles, and D. Michel, Key Eng. Mater. **132–136**, 432 (1997).
7. P. N. Martynov, R. Sh. Askhadullin, P. A. Yudintsev, and A. N. Khodan, Nov. Prom. Tekhnol., No. 4, 48 (2008).
8. J.-L. Vignes, C. Frappart, T. Di Costanzo, et al., J. Mater. Sci. **43**, 1234 (2008).
9. V. E. Asadchikov, R. S. Askhadullin, V. V. Volkov, et al., JETP Lett. **101**, 556 (2015).
10. G. Goerigk and Z. Varga, J. Appl. Crystallogr. **44**, 337 (2011).
11. A. Radulescu, E. Kentzinger, J. Stellbrink, et al., Neutron News **16**, 18 (2005).
12. G. D. Wignall and F. S. Bates, J. Appl. Crystallogr. **20**, 28 (1987).
13. http://iffwww.iff.kfa-juelich.de/~pipich/dokuwiki/doku.php/qtikws.
14. W. Schmatz, T. Springer, J. Schelten, and K. Ibel, J. Appl. Crystallogr. **7**, 96 (1974).
15. http://www.esrf.eu/computing/scientific/FIT2D/.
16. P. Euzen, P. Raybaud, X. Krokidis, et al., *Handbook of Porous Solids,* Ed. by F. Schüth, (Wiley-VCH, Weinheim, 2008).
17. S. Brunauer, L. S. Deming, W. E. Deming, and E. Teller, J. Am. Chem. Soc. **62**, 1723 (1940).
18. J. H. De Boer, *The Structure and Properties of Porous Materials* (Colston Papers, London, 1958), p. 68.
19. P. Debye and A. M. J. Bueche, Ann. Phys. (N. Y., NY, U. S.) **20**, 518 (1949).
20. V. Luzzati, Acta Crystallogr. **13**, 939 (1960).
21. O. Kratky, Prog. Biophys. Mol. Biol. **13**, 105 (1963).
22. *Small-Angle X-ray Scattering,* Ed. by O. Glatter and O. Kratky (Academic Press, London, 1982), p. 155.
23. R. P. Hjelm, P. Thiyagarajan, and H. Alkan-Onyuksel, J. Phys. Chem. **96**, 8653 (1992).
24. P. D. Southon, J. R. Bartlett, J. L. Woolfrey, and B. Ben-Nissan, Chem. Mater. **14**, 4313 (2002).
25. G. Beaucage, T. A. Ulibarri, E. P. Black, and D. W. Schaefer, in *ACS Symposium Series,* Vol. 585: *Hybrid Organic-Inorganic Composites,* Ed. by J. Mark, et al. (American Chemical Society, Washington DC, 1985), p. 97.
26. M. Štěpánek, P. Matějíček, K. Procházka, et al., Langmuir **27**, 5275 (2011).
27. T. V. Khamova, O. A. Shilova, G. P. Kopitsa, V. Angelov, A. Zhigunov, J. Surf. Invest.: X-ray, Synchrotron Neutron Tech. **10** (1), 113 (2016).
28. B. Hammouda, J. Appl. Crystallogr. **43**, 716 (2010).
29. P. W. Schmidt, D. Avnir, D. Levy, et al., J. Chem. Phys. **94**, 1474 (1991).
30. J. Teixera, in *On Growth and Form. Fractal and Non-Fractal Patterns in Physics,* Ed. by H. E. Stanley and N. Ostrovsky (Martinus Nijloff Publ., Boston, 1986), p. 145.
31. G. Porod, Kolloid-Z. **125**, 51 (1952).
32. G. Porod, Kolloid-Z. **125**, 109 (1952).
33. P. Wong, Phys. Rev. B **32**, 7417 (1985).
34. P. W. Schmidt, *Modern Aspects of Small-Angle Scattering,* Ed. by H. Brumberger (Kluwer Academic Publ., Dordrecht, 1995), p. 1.
35. Guinier, A. and Fournet, G., *Small Angle Scattering of X-rays* (John Wiley and Sons, New York, 1955).
36. G. Beaucage, J. Appl. Crystallogr. **28**, 717 (1995).
37. N. N. Gubanova, A. Ye. Baranchikov, G. P. Kopitsa, et al., Ultrason. Sonochem. **24**, 230 (2015).

Translated by E. Khozina

SPELL: 1. OK